



43
44 The ASB has a widespread distributed hydrological network with almost 200 ‘lake-like’
45 or water accumulation features. There may be a hydrological flow pathway operating
46 from subglacial lakes near the Dome C ice divide and the coast via the Totten Glacier
47 (Wright et al., 2012), potentially affecting the stability of the Totten Glacier.
48
49 Basal melting may contribute to subglacial hydrological flow. Basal meltwater
50 lubricates the flow of ice, which can impact the stability of the ice sheet and the
51 direction of the ice flow (Livingstone et al., 2016; Bell et al., 2007). The basal meltwater
52 moves down the pressure gradient and gradually develops into a complex subglacial
53 hydrological system, which eventually flows into the ocean (Fricker et al., 2016).
54 However, the spatial structure of the basal thermal state and basal melting rates beneath
55 the Totten Glacier are not yet well understood.
56
57 Basal melting can occur where the ice temperature reaches the pressure melting point,
58 dramatically lowering the basal friction and allowing the ice to flow faster. Geothermal
59 heat flux (GHF) is an important boundary condition for ice temperature. Its magnitude
60 and distribution affect the distribution of basal ice temperature and thus ice flow. The
61 magnitude of GHF depends on the spatially varying geological conditions that control
62 heat generation and conduction, including heat flux from the mantle, crustal thickness,
63 heat production in the crust by radioactive decay, groundwater flow, and tectonic history
64 (Pollack et al., 1993; Pittard et al., 2016). It is difficult to measure GHF directly due to
65 limited access to Antarctic bedrock, with only a few point measurements in ice-free
66 areas or from boreholes through the ice (Fisher et al., 2015). GHF datasets are
67 commonly estimated from models relying on either seismic (Shapiro and Ritzwoller,
68 2004; An et al., 2015; Shen et al., 2020), airborne magnetic data (Martos et al., 2017),
69 or satellite geomagnetic data (Fox-Maule et al., 2005; Purucker et al., 2013).
70
71 Previous thermomechanical simulations of Totten Glacier (Dow et al., 2020; Pattyn et
72 al., 2010; Pittard et al., 2016; Van Liefferringe et al., 2018) have used GHF data from
73 Shapiro and Ritzwoller (2004), Purucker et al. (2013) and An et al. (2015), but Wright
74 et al. (2012) used spatially uniform values. In this study, we simulated the basal thermal
75 state of Totten Glacier, based on the best available topographic data and five different
76 GHFs, including three GHF listed above, plus more recent GHF fields from Martos et
77 al. (2017) and Shen et al. (2020).
78
79 We apply an off-line coupling between a basal energy and water flow model and a 3D
80 full-Stokes ice flow model for each of the 5 GHF maps, to provide the best-fit
81 distribution of modelled basal temperature and basal melt rate. We evaluate the
82 simulated basal temperature fields under the different GHF maps using the observations
83 of water at the ice base to infer which GHF map is most reliable in the ASB. The
84 observations include a set of subglacial lakes locations and the specular content (Dow
85 et al., 2020) calculated from airborne radar data collected by the International
86 Collaborative Exploration of the Cryosphere by Airborne Profiling (ICECAP) survey.



87 Specularity is a parameterization of the along-track radar bed reflection scattering
88 function that has been used to provide an attenuation-independent proxy for distributed
89 subglacial water bodies (Schroeder et al., 2013). We devise measures of specularity that
90 help discriminate between alternative GHF maps to best characterize both cold and
91 warm beds.

92

93 **2 Regional Domain and Datasets**

94 Our modeled domain, the Totten Glacier, is located in the Aurora Subglacial Basin in
95 East Antarctica (Fig. 1). Its boundary is based on drainage-basin boundaries defined
96 from satellite ice sheet surface elevation and velocities (Mouginot et al., 2017). The
97 surface elevation, bedrock elevation, and ice thickness are from MEaSURES
98 BedMachine Antarctica, version 2 with a resolution of 500 m (Morlighem et al., 2020).

99

100 Simulation input and comparison datasets are shown in Table 1. The surface ice velocity
101 data are obtained from MEaSURES Phase-Based Antarctica Ice Velocity Map, Version
102 2 with resolution of 450 m (Rignot et al., 2017), which were mainly collected during
103 the International Polar Years from 2007 to 2009 with additional surveys between 2013
104 and 2016. Ice sheet surface temperature is prescribed by ALBMAP v1 with a resolution
105 of 5 km (Le Brocq et al., 2010) and comes from monthly estimates inferred from
106 AVHRR data averaged over 1982-2004 (Comiso, 2000). Subglacial lake locations are
107 from the fourth inventory of Antarctic subglacial lakes (Wright and Siegert, 2012) and
108 the first global inventory of subglacial lakes (Livingstone et al., 2022).

109

110 Five GHF datasets (Fig. 2; Table 2) are used in this study. All the datasets are
111 interpolated into 2.0 km resolution. The specularity content data are from Dow et al
112 (2020), where they calculated radar specularity content over ASB from the ICECAP
113 survey lines, and smoothed the data with a 1 km filter, following the equations described
114 in Schroeder et al. (2015). Specularity content is given as a relative value between 0
115 and 1, larger values mean a higher likelihood of the presence of water, and value of 0.4
116 is taken as the division where specularity content shows the presence of water (Young
117 et al., 2016).

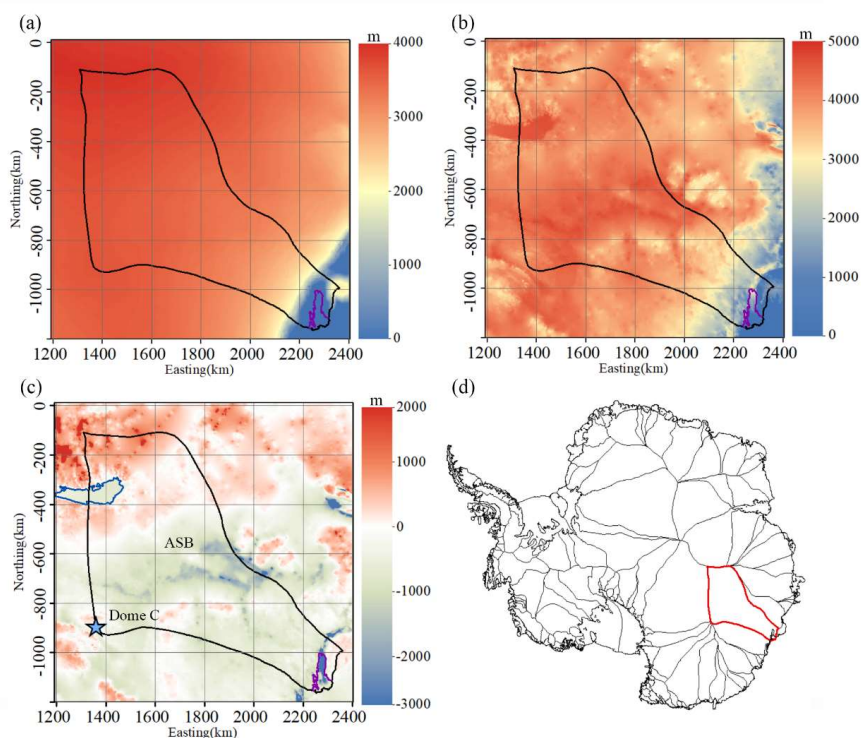
118

119 **Table 1 Datasets used in simulations.**

Variable name	Dataset	Resolution	Reference
surface elevation, bedrock elevation, and ice thickness	MEaSURES BedMachine Antarctica version 2	500 m	Morlighem et al., 2020; Cui et al., 2020
surface ice velocity	MEaSURES InSAR-based Antarctic ice velocity Map, version 2	450 m	Rignot et al., 2017
surface temperature	ALBMAP v1	5 km	Le Brocq et al., 2010
subglacial lake location	The first global inventory of subglacial lakes	-----	Livingstone et al., 2022
specularity content	Aurora Subglacial Basin GlADs inputs, outputs and geophysical data	1 km along track	Dow et al., 2019



120

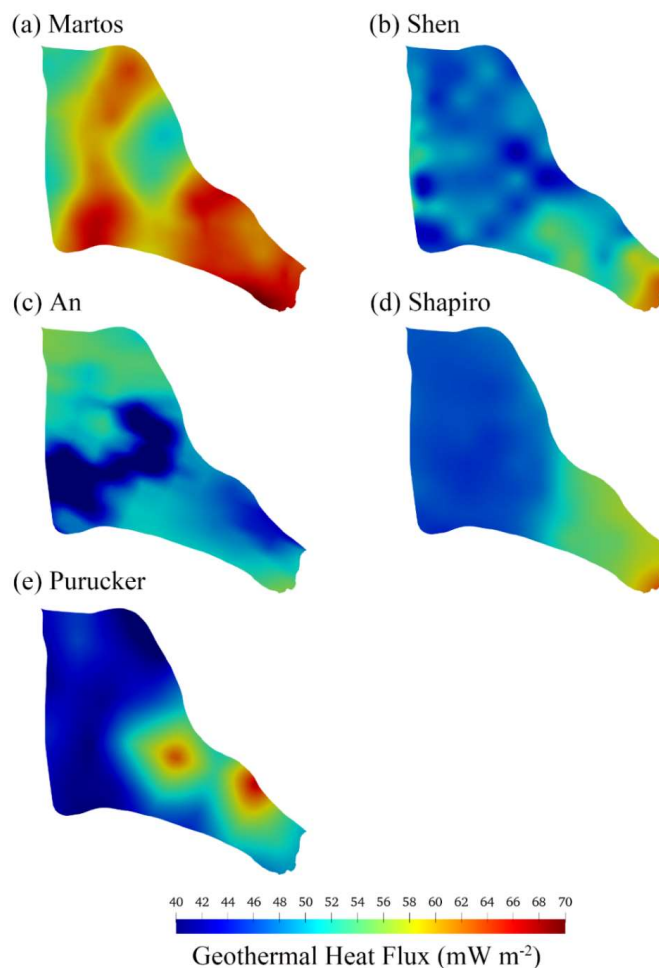


121

122 Fig. 1. The domain topography and location with domain boundary overlain. (a) surface elevation;
 123 (b) ice thickness; (c) bed elevation; (d) the location of our domain in Antarctica. The solid black
 124 curve is the outline of the study domain, including the Totten ice shelf. The purple curve in (a-c) is
 125 the grounding line of Totten glacier. The blue curve in (c) is Lake Vostok (Studinger et al., 2003).
 126 The solid red curve in (d) is the boundary of Totten Glacier. ASB and Dome C (blue star) are marked
 127 in (c).
 128

129 Table 2 The five GHF datasets used with the mean and range in our region.

GHF map	Reference	Method	Mean (mW m^{-2})	Range (mW m^{-2})
Martos	Martos et al., 2017	airborne geomagnetic data	65	51-70
Shen	Shen et al., 2020	seismic model	58	42-63
An	An et al., 2015	seismic model	51	34-56
Shapiro	Shapiro and Ritzwoller, 2004	seismic model	58	44-63
Purucker	Purucker, 2013	Satellite geomagnetic data	51	37-67



130

131 Fig. 2. The spatial distribution of GHF over our domain as described in Fig. 1. See Table 2 for the
132 GHF map details.

133

134 3 Model

135 Our goal is to map the basal thermal state of Totten glacier, including basal temperature
136 and basal melting rate. GHF, basal frictional heat and englacial heat conduction are the
137 main factors that determine the basal thermal state of the ice sheet. We need to simulate
138 the ice flow velocity and stress to calculate the basal frictional heat, and to simulate the
139 ice temperature to calculate the englacial heat conduction flux.

140

141 Following the same method as Kang et al. (2022), we solve an inverse problem by a
142 full-Stokes model, implemented in Elmer/Ice, to infer the basal friction coefficient such
143 that the modelled velocity best fits observations. To get a proper vertical ice temperature
144 profile subject to thermal boundary conditions needed in solving the inverse problem,

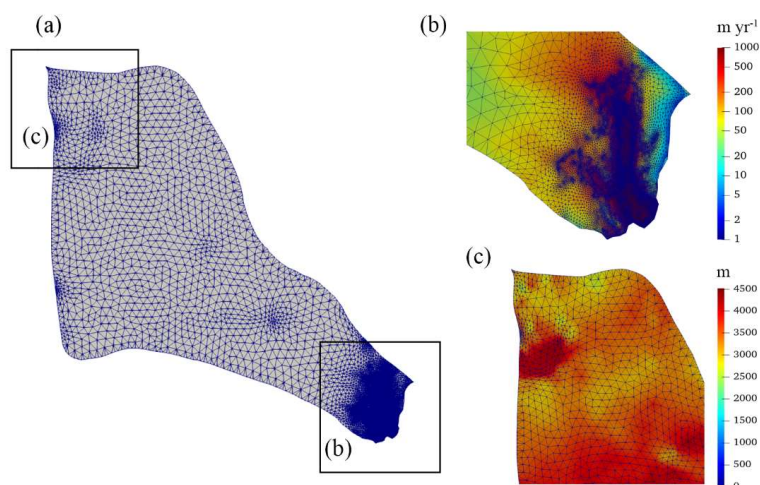


145 we use a forward model that consists of an improved Shallow Ice Approximation (SIA)
146 thermomechanical model with a subglacial hydrology model (Wolovick et al., 2021a).
147 We do steady state simulations by coupling the forward and inverse models.

148

149 3.1 Mesh Generation and Refinement

150 We use GMSH (Geuzaine and Remacle, 2009) to generate an initial 2-D horizontal
151 footprint mesh. Then we refine the mesh by an anisotropic mesh adaptation code in the
152 Mmg library (<http://www.mmgtools.org/>). The resulting mesh is shown in Fig. 3 and
153 has minimum and maximum element sizes of about 800 m and 20 km. The range of
154 mesh size is 800 m at ice shelf, 1-3 km upstream near the grounding line, and 6-20 km
155 over most of the inland ice. The 2-D mesh is then vertically extruded using 10 equally
156 spaced, terrain following layers.



157

158 Fig. 3. The refined 2-D horizontal domain footprint mesh (a). Boxes outlined in (a) are shown in
159 detail overlain with surface ice velocity in (b) and with ice thickness in (c).

160

161 3.2 Boundary Conditions

162 The ice surface is assumed to be stress-free. At the ice front, the normal stress under the
163 sea surface is equal to the hydrostatic water pressure. On the lateral boundary, the
164 normal stress is equal to the ice pressure applied by neighboring glaciers and the normal
165 velocity is assumed to be 0. The bed for grounded ice is assumed to be rigid,
166 impenetrable, and fixed over time. For simplicity, we ignore the existence of Lake
167 Vostok and replace the lake with bedrock. We do this to avoid having to implement a
168 spatially variable sea level in our model, as the level of hydrostatic equilibrium in Lake
169 Vostok is several thousand meters higher than in the ocean. Our inverted drag
170 coefficient over the lake is very low, indicating that our simplification has only a small
171 influence on ice flow. However, our basal melt rates over the lake are probably
172 inaccurate, as we assume that geothermal flux from the lake bottom is applied directly



173 to the ice base, without accounting for circulation within the lake.
174 A linear sliding law is used to describe the relationship between the basal sliding
175 velocity and the basal shear force, on the bottom of grounded ice,

$$\tau_b = C \cdot u_b, \quad (1)$$

176 To avoid non-physical negative values, $C = 10^\beta$ is used in the simulation. We call β
177 the basal friction coefficient. C is initialized to a constant value of 10^{-4} MPa m⁻¹ yr
178 (Gillet-Chaulet et al., 2012), and then replaced with the inverted C in subsequent
179 inversion steps.

180
181 We relax the free surface of the domain by a short transient run to reduce the non-
182 physical spikes in initial surface geometry (Zhao et al., 2018). The transient simulation
183 period here is 0.5 yr with a timestep of 0.01 yr.

184
185 Following the same method as Kang et al. (2022), we improve the parameterization of
186 β via C in Eq 5 (Section 3.2.2) by considering basal temperature T_{bed} ,

$$\beta_{new} = \beta_{old} + \alpha(T_m - T_{bed}), \quad (2)$$

187 where β_{old} is from the inverse model, α is a positive factor to be tuned, T_m is pressure
188 melting temperature. We take α to be 1, and use the parameterization of β_{new} in Eq 1
189 in all the simulations (Kang et al., 2022). Using Eq 2 does not change simulated surface
190 velocities in the interior region.

191

192 3.3 Basal Melt Rate

193 Based on the inverted basal velocity and basal shear stress, we can calculate the basal
194 friction heat. We then produce the basal melt rate using the thermal equilibrium as
195 follows (Greve and Blatter, 2009):

$$M = \frac{G + \vec{u}_b \vec{\tau}_b + k(T) \frac{dT}{dz}}{\rho_i L}, \quad (3)$$

196 where M is the basal melt rate, G is GHF, $\vec{u}_b \vec{\tau}_b$ is the basal friction heat, $-k(T) \frac{dT}{dz}$ is the
197 upward heat conduction, ρ_i is the ice density, and L is latent heat of ice melt. GHF and
198 frictional heating from basal slip warm the base, while the upward heat conduction to
199 the interior cools the base.

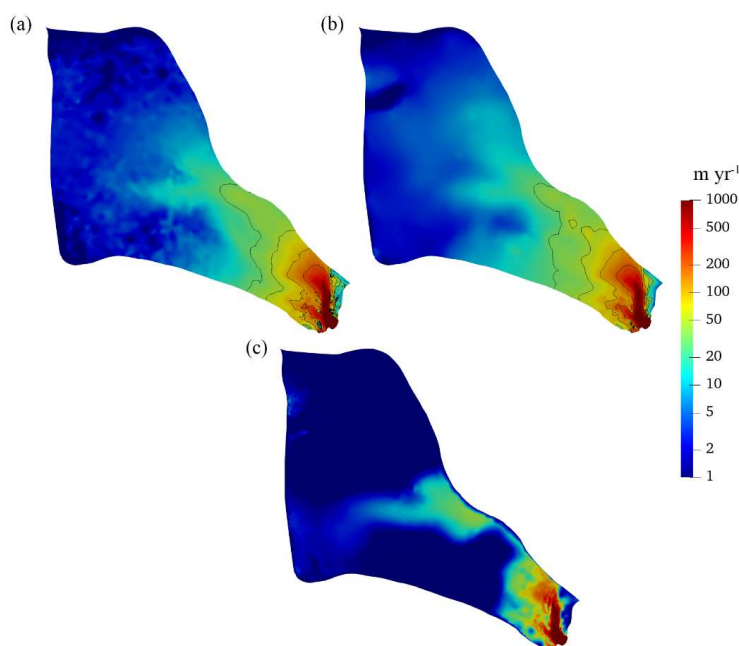
200 4 Simulation Results

201 4.1 Ice Velocity

202 The modeled surface velocity fields with different GHFs are all very close to the
203 observed as expected by design of the minimization of misfit between the modeled and
204 the observed surface velocity in the inverse model. Therefore, we show only the Martos
205 et al. (2017) result as a representative example of all simulated velocity fields (Fig. 4).



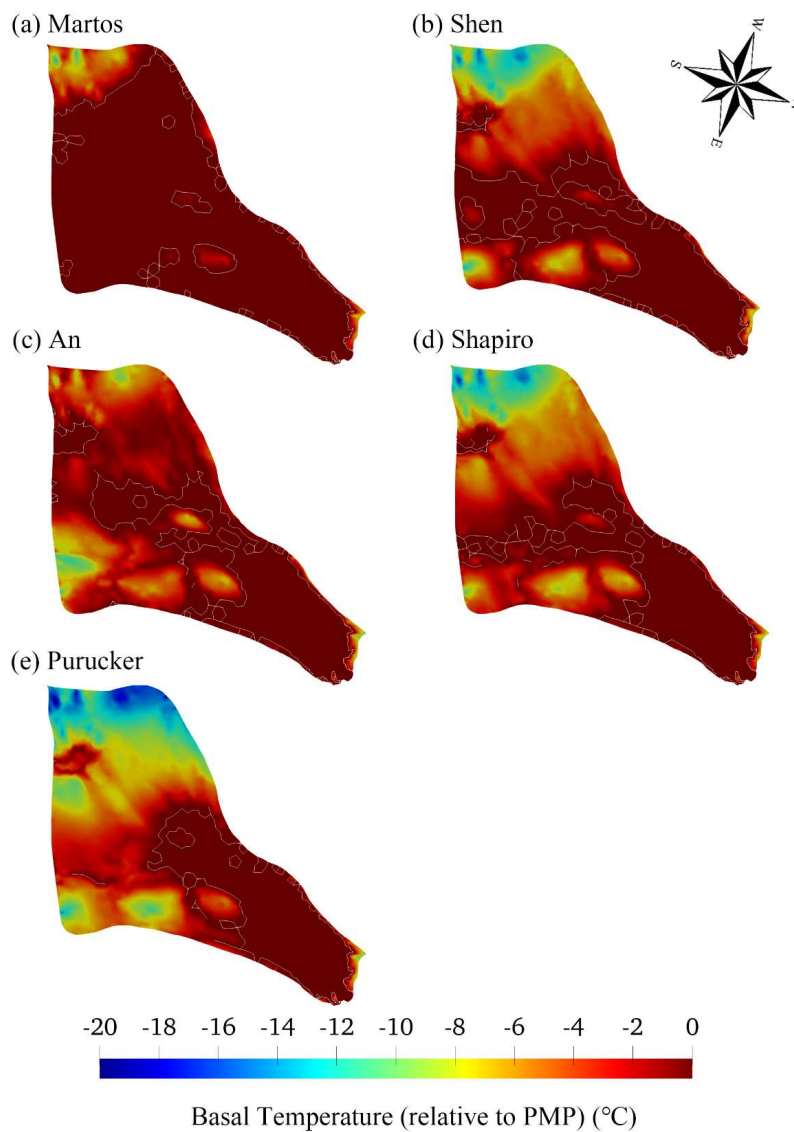
206 The surface speed can reach as high as about 1000 m yr^{-1} on the ice shelf (Fig. 4a, b).
207
208 Fig. 4c shows the modeled basal ice velocity. The modeled basal ice velocity is close to
209 0 in most of the inland region. The fast basal velocity in the middle of the region (Fig.
210 4c) is associated with subglacial canyon features (Fig. 1c), high basal temperature (Fig.
211 5) and small friction coefficient. In the grounded fast flow region, the basal ice velocity
212 can reach a maximum of 500 m yr^{-1} .



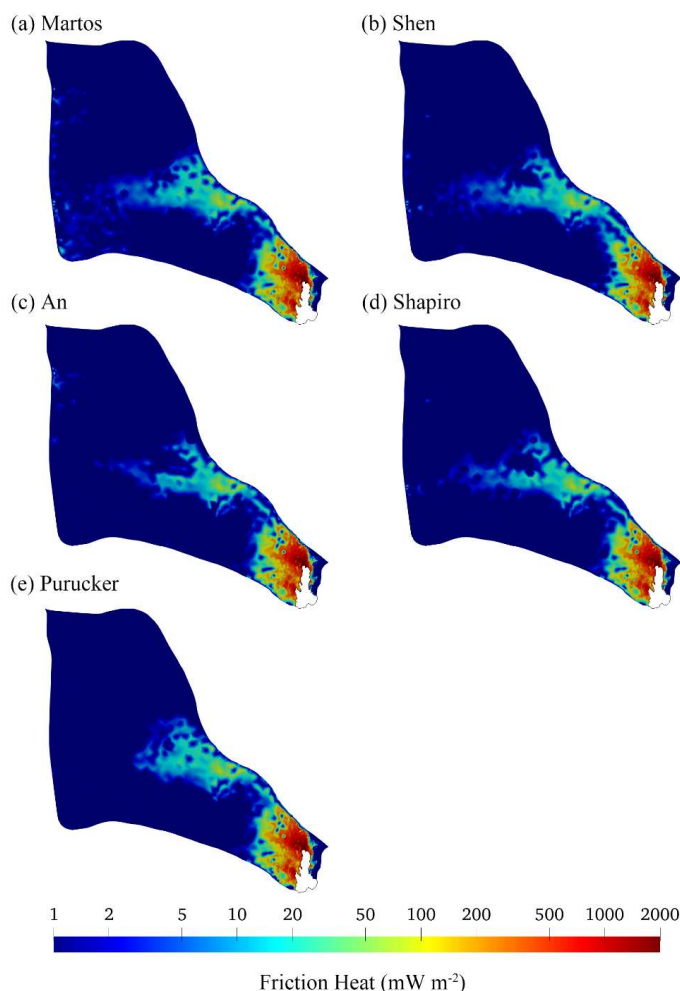
213
214 Fig. 4. (a) Observed surface velocity, (b) modeled surface velocity, (c) modeled basal velocity in the
215 experiment using the Martos et al. (2017) GHF. The black solid lines in (a) and (b) represent speed
216 contours of 30, 50, 100 and 200 m yr^{-1} .
217

218 4.2 Basal Ice Temperature, Basal Friction Heat and Heat Conduction

219 Fig. 5 shows the modelled basal temperatures from the five experiments. In the fast-
220 flowing region (defined as having surface speeds higher than 30 m yr^{-1}), the modelled
221 ice basal temperatures are all at the pressure melting point (“warm”). However, in the
222 slow-flowing region, the modeled ice basal temperature shows large difference between
223 GHF fields. In the experiment using the Martos et al. (2017) GHF (Fig. 5a), which has
224 the highest GHF over the domain, we get the largest area of warm base extending to all
225 but the inland southeast corner. The experiment using Shen et al. (2020) GHF (Fig. 5b),
226 which has the second highest GHF, yields the second largest area of warm base. The
227 experiment using Purucker et al. (2013) GHF (Fig. 5e), with the lowest GHF has the
228 smallest warm base area, which is mostly confined to the fast-flowing region. All
229 experiments show cold basal temperatures in the southwest corner which is associated
230 with relatively thin ice above subglacial mountains (Fig. 1c).



231
232 Fig. 5. Modelled basal temperature relative to pressure melting point, (a) to (e) corresponding to the
233 GHF (a) to (e) in Fig. 2. The ice bottom at the pressure-melting point is delineated by a white contour.
234



235

236 Fig. 6. Modelled basal friction heat.

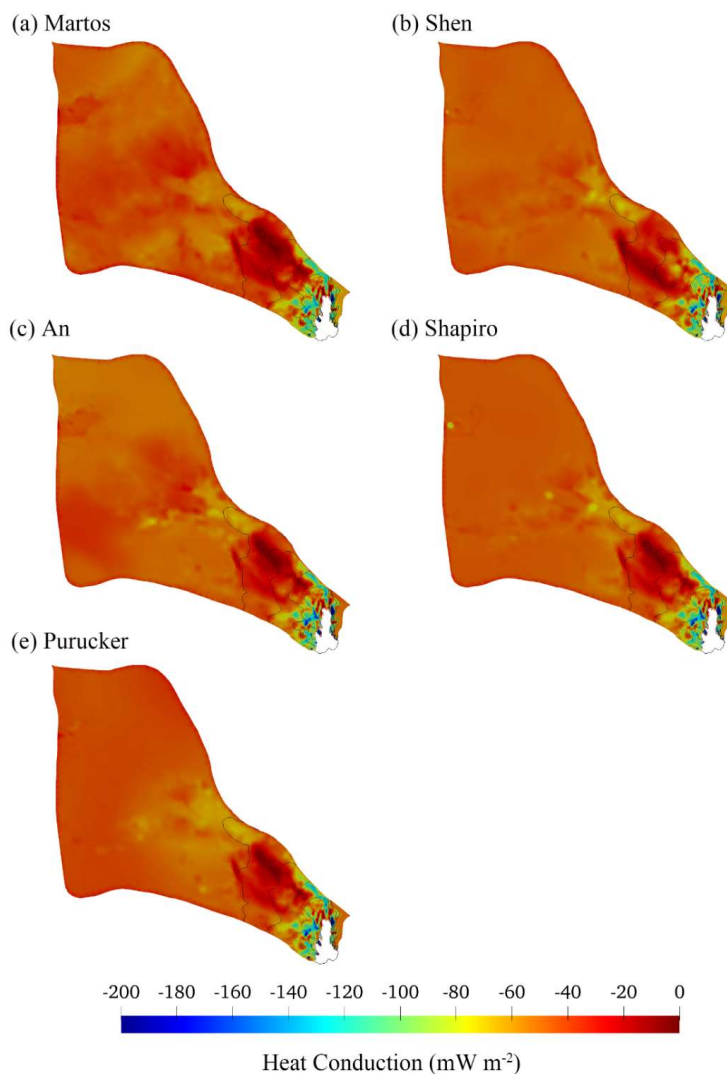
237

238 The distribution of modeled basal friction heat is closely associated with that of
239 modelled basal velocity. The patterns of basal friction heat with different GHFs are very
240 similar in fast flow region, but have some differences in the middle of the domain (Fig.
241 6) where modelled basal velocity ranges between 5-20 m yr^{-1} (Fig. 4).

242

243 The modelled basal friction heat is close to 0 where the surface ice velocity is less than
244 10 m yr^{-1} , but ranges widely by 10-2000 mW m^{-2} elsewhere. Basal friction heating
245 larger than 100 mW m^{-2} occurs where surface velocity is more than 50 m yr^{-1} and basal
246 velocity is higher than 10 m yr^{-1} (Fig. 6; Fig. 4), and it is then the dominant heat source.

247



248

249 Fig. 7. Modelled heat change of basal ice by upward englacial heat conduction. The negative sign
250 means that the upward englacial heat conduction causes heat loss from the basal ice as defined by
251 the color bar with cooler colors representing more intense heat loss by conduction. (a) to (e)
252 corresponding to the GHF (a) to (e) in Fig. 2. The black solid curves represent modelled surface
253 speed contours of 30, 50, 100 and 200 m yr^{-1} , as in Fig. 4.

254

255 Fig. 7 shows the modeled heat change of basal ice by upward englacial heat conduction
256 in the five experiments. In the slow-flowing region where basal temperature is below
257 the pressure melting point, the upward basal heat conduction equals the GHF (Fig. 5,
258 Fig. 7). In the region where basal temperature reaches pressure melting point (Fig. 5)



259 with low basal velocity (Fig. 4c) and thick ice (≥ 2500 m; Fig. 1c), the heat loss caused
260 by upward basal heat conduction is < 30 mW m⁻² in all experiments (Fig. 7), reflecting
261 the development of a temperate basal layer that limits the basal thermal gradient. In the
262 fast-flowing tributaries with high basal velocity (Fig. 4c) and ice thickness < 2000 m,
263 the heat loss caused by upward basal heat conduction can be very large, 100-200 mW
264 m⁻² near the grounding line (Fig. 7).

265

266 **4.4 Basal Melt Rate**

267 We calculate basal melt rate using the thermal balance equation (Eq 3). There are
268 significant differences in the five experiments due to large variability in GHF (Fig. 8).
269 The Martos et al. (2017) and then Shen et al. (2020) yield the largest areas with basal
270 melting. The experiments using An et al. (2015), Shapiro and Ritzwoller (2004) and
271 Purucker et al. (2013) yield similar total basal melting areas but have different spatial
272 patterns.

273

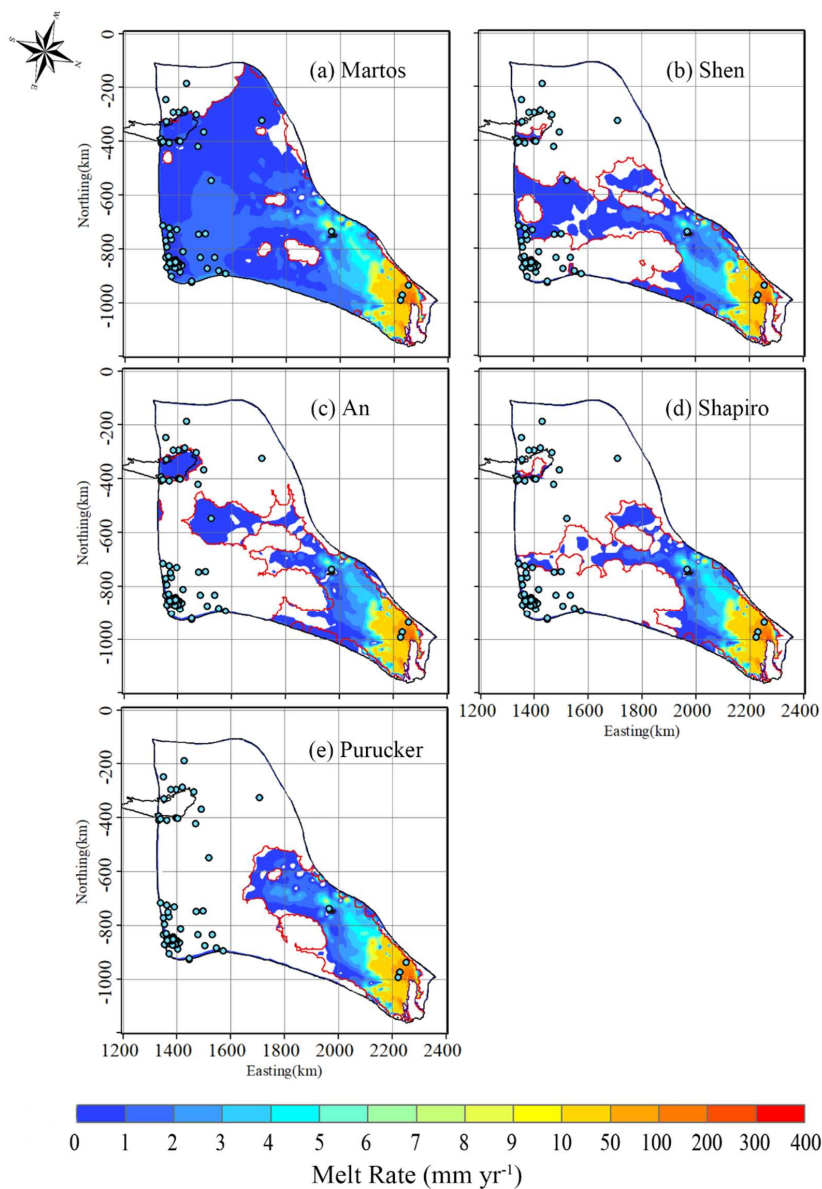
274 In most of the warm based regions, the modeled basal melting rate is < 5 mm yr⁻¹ (Fig.
275 8) and basal friction heat is < 50 mW m⁻² (Fig. 6). Basal melting rates > 5 mm yr⁻¹ occur
276 with surface velocities > 100 m yr⁻¹ (Fig. 4, Fig. 8), where the basal friction heat is the
277 dominant heat source. In particular, the modeled basal melting rate is 50-400 mm yr⁻¹
278 in the two fast flow tributaries feeding the ice shelf that have surface velocities > 200
279 m yr⁻¹, and where the basal friction heat can reach 500-2000 mW m⁻² (Fig. 4, Fig. 6, Fig.
280 8). This is consistent with the findings of Larour et al. (2012) and Kang et al. (2022),
281 that the slow-flowing ice is more sensitive to GHF while the fast-flowing region is more
282 sensitive to basal friction heat.

283

284 There is relatively high modelled basal melt rate (4-10 mm yr⁻¹) localized at the central
285 subglacial canyon (Fig. 8, Fig. 1c), which is captured by all five GHF experiments, and
286 also consistent with the high values (0.5-1.0) of specularly content data there (Fig. 9).
287 Dow et al. (2020) found that the specularly content is a useful proxy for both water
288 depth and water pressure in regions of distributed water in subglacial canyons.

289

290 There is a location with modelled refreezing (negative melting rate) at the central
291 subglacial canyon, near the observed subglacial lake, in all five GHF experiments (Fig.
292 8). The value of specularly content there is low as 0-0.1 (Fig. 9), and freeze on is driven
293 by the steep topography around the canyon.



294

295 Fig. 8. Modelled basal melt rate, (a) to (e) correspond to the GHF (a) to (e) in Fig. 2. The ice bottom
296 at pressure-melting point is surrounded by a red contour. The black curve denotes Lake Vostok.
297 Stable subglacial lakes are shown as blue-green points with black circles. There is modelled basal
298 refreezing at the central canyon painted in black.

299

300 4.5 Evaluation of modelled results with 5 GHFs

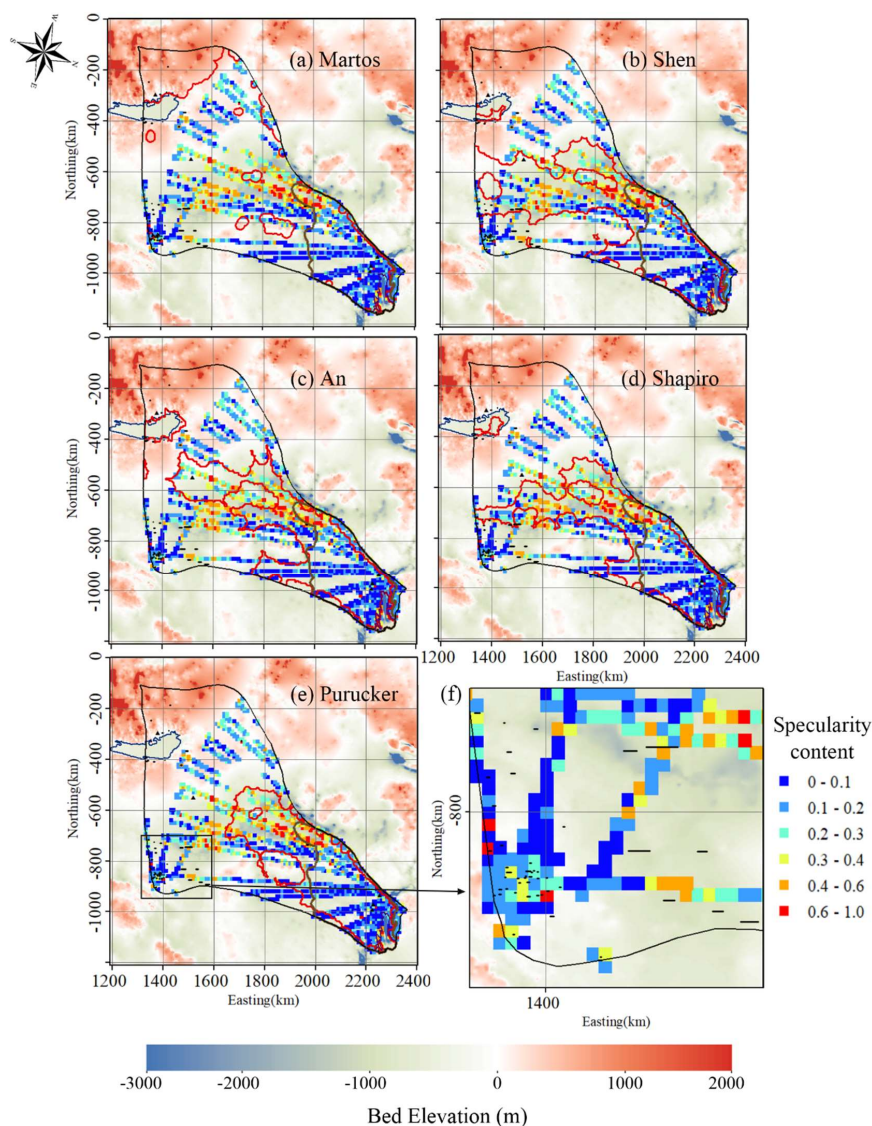
301 We use the locations of the observed subglacial lakes and specularity content to



302 discriminate between modeled basal melting (Fig. 8). Ideally, we would like to have a
303 modeled ice base that is cold and dry where subglacial lakes do not exist and the
304 specularity content is low, and a modeled ice base that is at the melting point where
305 lakes and high specularity content are observed. In other words, we would like to use
306 the available data to form a two-sided constraint that can penalize the model for being
307 both too warm and too cold. If we only have a one-sided constraint, then we would
308 always end up concluding that either the warmest or the coldest GHF map is best,
309 regardless of whether that map was a reasonable representation of the basal state.

310
311 Observations of subglacial lakes are mostly a one-sided constraint on the basal thermal
312 state. This is because lakes are only detectable if subglacial water accumulates in
313 depressions that are deep compared to the radar wavelength and wide in comparison to
314 the horizontal resolution of the radar system. Other forms of distributed hydrology,
315 such as linked cavities or saturated subglacial sediments, do not produce the classic flat
316 bright reflectors characteristic of subglacial lakes. Thus, the lack of observed subglacial
317 lakes in a particular region cannot be taken as evidence that there is no subglacial water
318 there. The mesh resolution of our model inland is about 20 km (Fig. 3). But 84% of the
319 subglacial lakes have along-radar track lengths below 5 km, 94% are below 10 km, with
320 only 5 lakes including Lake Vostok above 10 km (Fig. 9f). So the subglacial lakes may
321 be too small for the ice model to resolve. Nonetheless, we compare our modeled basal
322 thermal state with the observed locations of subglacial lakes. These comparisons show
323 that all the experiments can capture all four subglacial lakes in the fast-flowing region
324 (Fig. 8). But their performance in covering subglacial lakes in the slow-flowing region
325 differ greatly.

326
327 In addition to the subglacial lakes, we use specularity content to derive a two-sided
328 constraint on basal thermal state. Specularity content is an inherently noisy measure, so
329 it is smoothed to 1 km along track values, and furthermore it is not unambiguously an
330 indicator of wet beds. For example, specularity content is low in the fast-flowing region
331 (Fig. 9, Fig. 4), where there must be lubricating water at the bed. Similar specularity
332 results were also seen by Schroeder et al. (2013) for Thwaites Glacier, where high
333 specularity values are seen under the major tributaries and the upstream trunk, but
334 significant lower values of specularity in the fast-flowing region. This counter-intuitive
335 result may be due to distinct morphologies and radar scattering signatures between
336 water distributed in widespread subglacial conduits and water concentrated in just a few
337 subglacial channels. Because of this effect, we only use the specularity content outside
338 the fast-flowing region (defined as surface speed $>30 \text{ m a}^{-1}$, Fig. 9).



339
340 Fig. 9. Locations of specularity content (colored points) derived from radar data collected by
341 ICECAP (Dow et al., 2020) and interpolated to 10 km by 10 km grids under the background of
342 bedrock elevation. Specularity content > 0.4 indicates the likely presence of basal water. The ice
343 bottom at pressure-melting point is surrounded by a red contour, (a) to (e) correspond to the five
344 GHF maps (a) to (e) in Fig. 2. Lake Vostok is outlined by a blue curve. The brown curve is the
345 contour of surface speed of 30 m a^{-1} . Subglacial lakes are shown at observed positions as a line
346 segment of their length. Plot (f) is a zoom of the box in plot (e).
347
348 The specularity content data calculated from ICECAP survey lines suggests hundreds
349 of locations with basal water (Dow et al., 2020). The default resolution of specularity



350 content along the flight lines is 1 km (Dow et al., 2020), which is smaller than our model
351 resolution of 6-20 km in the slow flowing region. Water may accumulate in just a small
352 fraction of the grid cell even if the majority of the cell is warm because of water flow.
353 For comparability, with our simulation resolution we aggregated the specularity content
354 data onto 10 km by 10 km windows (Fig. 9). The 10 km window is a somewhat arbitrary
355 choice, but smaller windows (we tried 2 and 5 km) reduce the data available and noise
356 becomes larger, while larger windows (we tried 15 and 20 km) restrict spatial resolution.
357 We then take the upper fifth percentile of the specularity content, $specularity_5$ of each
358 window as a water indicator rather than its mean value to allow for localized water
359 collection or unfavorable bed reflection geometry, while also excluding spurious signals
360 in the noisy specularity data. Young et al. (2016) suggested that specularity larger than
361 0.4 was an indicator of a warm bed. This is also consistent with the largest subglacial
362 lake in the domain with length of 28 km having specularity content >0.4 (Fig. 9f). There
363 are also some smaller lakes (several km along-track lengths) with specularity content
364 between 0.2 and 0.4, so a warm threshold of 0.4 would not capture these features. The
365 cold threshold need not be the same as the warm bed one, and so we explored different
366 values for cold thresholds of 0.2, 0.3, 0.4, but found that the 0.2 cold threshold provided
367 best discrimination between models, and also maximizes the available data.

368
369 To evaluate modelled basal conditions with specularity content, we define a warm hit
370 rate as the ratio of the number of grid cells with modelled warm bed that have
371 $specularity_5 > 0.4$ to the total number of grids with $specularity_5 > 0.4$. Similarly, cold
372 hit rate is defined as the ratio of the number of grid cells with $specularity_5 < 0.2$.

373
374 One simple measure of quality is just the average of warm hit rate and cold hit rate, but
375 we also want an unbiased evaluation of GHF to have similar capabilities in capturing
376 both warm bed and cold bed regions. Therefore, we define *imbalance* as

377
$$imbalance = \frac{warm\ hit\ rate - cold\ hit\ rate}{warm\ hit\ rate + cold\ hit\ rate},$$

378 as it reflects the difference between warm hit rate and cold hit rate, and has a value
379 between -1 and 1. The closer to zero *imbalance* is, the more confidence we have in the
380 model result. The overall performance is estimated by averaged hit rate minus the
381 absolute value of *imbalance*.

382
383 The Martos GHF has the highest warm hit rate and the lowest cold hit rate since it has
384 the largest modelled warm bed area. The averaged hit rates of modelled results with 5
385 GHF are very close, with differences < 0.13 (Table 3). The Shapiro, Purucker, then Shen
386 have the highest averaged hit rate using all the values for threshold of cold bed, and the
387 differences between their averaged hit rate < 0.04 .

388
389 Martos and Shen have positive *imbalance*, which means that their warm hit rate is
390 higher than their cold hit rate. In contrast, An, Shapiro and Purucker have negative
391 *imbalance*. Martos has the largest *imbalance* because its warm hit rate overwhelms its
392 cold hit rate. The absolute *imbalance* of Shen is < 0.05 with all three cold hit thresholds



393 we used and always the smallest (Table 3) of the GHF. The Shapiro absolute *imbalance*
394 the second smallest with all the cold hit thresholds. Therefore, Shen and Shapiro rank
395 the top two according to *imbalance* between warm hit rate and cold hit rate.

396

397 Considering the overall performance by averaged hit rate minus the absolute value of
398 *imbalance*, Shen is the best, Shapiro the second, Purucker the third, An the fourth and
399 Martos the last (Table 3). The ranking is robust with all three cold hit thresholds.

400

401 Table 3. Warm hit rate, cold hit rate, averaged hit rate, imbalance and overall
402 performance for the modelled results with 5 GHFs. The threshold of *specularity*₅ is
403 taken as 0.4 for warm hit rate, and 0.2 for cold hit rate.

GHF	warm hit rate	cold hit rate	averaged hit rate	Imbalance	averaged hit rate – abs(imbalance)
Martos	0.9560	0.1648	0.56	0.71	-0.15
Shen	0.6588	0.6564	0.65	0.0018	0.65
An	0.4340	0.7652	0.60	-0.28	0.32
Shapiro	0.5975	0.7822	0.69	-0.13	0.56
Purucker	0.5283	0.8201	0.67	-0.22	0.45

404

405 **5 Discussion**

406 Wright et al. (2012) modelled basal temperature of Totten Glacier using the Glimmer
407 ice sheet model with a constant GHF of 54 mW m⁻². Their modelled area of basal warm
408 ice is between what we simulated using Martos et al. (2017) and Shen et al. (2020),
409 covering most of the lakes and lake-like features but missing some near Lake Vostok.
410 Dow et al. (2020) ran the Ice Sheet System Model (Larour et al., 2012) with a constant
411 GHF of 55 mW m⁻², producing a warm bed region slightly larger than we simulated
412 using the Shen et al. (2020) GHF (which has a mean of 58 mW m⁻² in this region, Table
413 2). Eisen et al. (2020) modeled the basal temperature of Antarctic ice sheet with the
414 Parallel Ice Sheet Model using four different GHF datasets (Shapiro and Ritzwoller,
415 2004; Fox Maule et al., 2005; An et al., 2015; Martos et al., 2017). The mean modelled
416 basal temperature of the different GHFs appear close to our result using the Shen et al.
417 (2020) GHF, with basal temperatures reaching the pressure melting point in the fast
418 flow region and the central upstream region of Totten Glacier.

419

420 Kang et al. (2020) evaluated basal thermal conditions underneath the Lambert-Amery
421 glacier system using six GHFs, and found that the two most recent GHF fields inverted
422 from aerial geomagnetic observations and which have the highest GHF values,
423 produced the largest warm-based area, and best matched the observed distribution of
424 subglacial lakes. This might be expected as there was only a one-sided constraint used,
425 and warm based models produced matches with more lakes.

426

427 Although the basal ice in fast-flowing regions is all at pressure melting point because
428 basal friction heat dominates the heat balance, the modelled basal melt rate of the



429 grounded ice in fast-flowing regions exhibits large differences across-models. The
430 modelled basal melt rate is associated with the modelled basal friction heat, which is a
431 function of the modelled basal velocity and basal shear stress, the accuracy of which
432 depends on the configuration and constraints of the ice sheet model used. Our modelled
433 maximum basal melt rate on the grounded ice is 0.4 m yr^{-1} near the grounding line. This
434 is close to the modelled maximum basal melt rate of 0.34 m yr^{-1} near the grounding line
435 by Dow et al. (2020), where they calculated the basal melt rates as a function of
436 combined GHF and frictional heating using the Ice Sheet System Model. We know of
437 no observations of the basal melt rates of grounded ice in Totten Glacier.

438
439 Modelled basal sliding speeds by Dow et al. (2020) range from 0.06 m yr^{-1} inland to
440 900 m yr^{-1} at the grounding line, which is close to our result (Fig. 4). Dow et al (2020)
441 simulate basal sliding generally where bedrock is below sea level, with an area close to
442 our simulation with a basal sliding coefficient β_{old} and which is larger than ours using
443 the improved basal sliding coefficient β_{new} (Eq 2) found by considering the basal
444 temperature relative to pressure-melting point. The modelled basal sliding speed
445 reaches a local maximum at the middle of the subglacial canyon system (Fig. 4), which
446 leads to local maxima in basal friction and basal melt rate (Fig. 8), and is consistent
447 with the high values of specularity (Fig. 9).

448
449 To evaluate the simulation results, we compare the simulated basal melting area with
450 the locations of the discovered subglacial lakes and specularity content derived from
451 radar data collected by ICECAP (Dow et al., 2020). Specularity is a parameterization
452 that estimates the along-track angularly narrow component of bed echo energy
453 compared with the isotropic diffuse energy component (Schroeder et al., 2015).
454 Specularity is determined by a set of ice/bed properties including the length, width and
455 thickness of the water body, its conductivity, and the roughness of the ice/water
456 interface. Off-nadir across-track reflectors may also produce glints creating noise in the
457 specularity distribution. Hence, interpretation of specularity is ambiguous and
458 dependent on the local bed morphology. This led us to experiment with a range of
459 windows over which to aggregate the bed reflection energy, and various thresholds for
460 estimating cold and warm beds. We were able to use the numerous subglacial lakes in
461 the region as a guide to setting these parameters, bearing in mind that the observations
462 of subglacial lakes are a one-sided constraint. If the modeled basal melting area misses
463 the subglacial lake or high specularity content, the model is underestimating the basal
464 temperature at that location. However, if the basal melting is simulated in areas without
465 observed subglacial lakes, it is unclear if this is because the models overestimate the
466 temperature in those areas, or if the water under the ice sheet has not been detected.
467 Moreover, a hypersaline lake and various other water saturated environments seem to
468 exist below cold ice beneath Devon Island ice cap in Canada (Rutishauser et al., 2022).
469 In addition, relatively high electrical conductivity beds like water saturated clays can
470 lead to false positives in radar detections of subglacial water bodies (Talalay et al.,
471 2020).

472



473 Our evaluation using specularly content is a two-sided constraint and thus improves on
474 observed subglacial lakes as a discriminating feature of cold and warm beds. The
475 experiment with Martos et al. (2017) GHF models the largest region of basal melt, and
476 covers most observed subglacial lake locations. However, it ranks worst in the
477 evaluation using specularly content, because it cannot capture cold beds well.

478

479 **6 Conclusions**

480 In this study we diagnose the basal thermal state of Totten Glacier by coupling a forward
481 model and an inverse model and using five different GHFs. By comparing modelled
482 basal temperature distributions with metrics derived from specularly content data we
483 evaluate the reliability of the five GHF data in this area.

484

485 We find there are significant differences in the spatial distributions of modelled
486 temperate ice with different GHFs, and the differences are mainly concentrated in the
487 slow ice flow regions. The modelled basal thermal state (frozen/melting) in the slow
488 ice flow region is mainly determined by the heat balance between GHF and englacial
489 upward heat conduction, and the basal melting rate is generally less than 5 mm yr^{-1} .
490 However, there is local maximum in modelled basal melt rate ($4\text{-}10 \text{ mm yr}^{-1}$) at the
491 central subglacial canyon, which could be explained by the local high basal sliding
492 velocity and frictional heat that are captured by all GHF experiments. This is consistent
493 with the high values of specularly content data there.

494

495 The basal heat balance in the fast ice flow region is mainly determined by the basal
496 frictional heat. The basal ice in the fast flow region is all at the melt point. The modeled
497 basal melting rate is $50\text{-}400 \text{ mm yr}^{-1}$ in the two fast flow tributaries feeding the ice shelf
498 with surface velocity greater than 200 m yr^{-1} , where the basal friction heat is $500\text{-}2000$
499 mW m^{-2} .

500

501 Our evaluation using specularly content as a two-sided constraint, gives quite different
502 result than only using observed locations of subglacial lakes. Simulations with the
503 Martos et al. (2017) GHF yields the largest region of basal melt, which covers most
504 observed subglacial lake locations, however, its cold bed fit with specularly content is
505 poor and shows huge imbalance in modelling warm bed and cold bed regions. Overall,
506 Martos et al. (2017) GHF ranks last in the evaluation with specularly content. Shen et
507 al. (2020) GHF yields the second largest area of basal melt and second best agreement
508 with the locations of the subglacial lakes, and also scores well in modelling both warm
509 and cold bed areas. Shen et al. (2020) GHF and Shapiro and Ritzwoller (2004) GHF
510 rank the top two according to the evaluation with specularly content. The best-fit
511 simulated result shows that most of the inland bed area is frozen. Only the upstream
512 subglacial canyon inland reaches pressure-melting point, and modelled basal melting
513 rate there is $0\text{-}10 \text{ mm yr}^{-1}$.

514

515 **Data availability**

516 MEaSURES BedMachine Antarctica, version 2, is available at



517 <https://doi.org/10.5067/E1QL9HFQ7A8M> (Morlighem, 2020). MEaSURES InSAR-
518 based Antarctic ice velocity Map, version 2, is available at
519 <https://doi.org/10.5067/D7GK8F5J8M8R> (Rignot et al., 2017). MEaSURES Antarctic
520 Boundaries for IPY 2007–2009 from Satellite Radar, version 2 is available at
521 <https://doi.org/10.5067/AXE4121732AD> (Mouginot et al., 2017). The subglacial lake
522 dataset is available at <https://doi.org/10.1038/s43017-021-00246-9> (Livingstone et al.,
523 2022). The specularly content dataset <https://doi.org/10.5281/zenodo.3525474> (Dow
524 et al., 2020). ALBMAP v1 and the GHF dataset of Shapiro and Ritzwoller (2004) are
525 available at <https://doi.org/10.1594/PANGAEA.734145> (LeBrocq et al., 2010b). The
526 GHF dataset of An et al. (2015) is available at
527 <http://www.seismolab.org/model/antarctica/lithosphere/AN1-HF.tar.gz> (last access: 11
528 April 2023). The GHF dataset of Shen et al. (2020) is available at
529 <https://sites.google.com/view/weisen/research-products?authuser=0> (last access: 11
530 April 2023). The GHF dataset of Martos (2017) is available at
531 <https://doi.org/10.1594/PANGAEA.882503>. The GHF dataset of Purucker (2012) is
532 available at http://websrv.cs.umt.edu/isis/index.php/Antarctica_Basal_Heat_Flux (last
533 access: 11 April 2023). The modelled basal temperature, basal melt rate and the upper
534 fifth percentile of the specularly content in this paper will be available at
535 <https://doi.org/10.5281/zenodo.7825456>.

536

537 **Author contributions.**

538 LZ and JCM conceived the study. LZ, MW, and JCM designed the methodology. YH,
539 LZ, and YM carried out the simulations and produced the estimates and figures. LZ
540 wrote the original draft, and all the authors revised the paper.

541

542 **Competing interests.**

543 The authors declare no conflict of interest.

544

545 **Acknowledgments**

546 This work was supported by the National Natural Science Foundation of China (No.
547 41941006), National Key Research and Development Program of China
548 (2021YFB3900105), State Key Laboratory of Earth Surface Processes and Resource
549 Ecology (2022-ZD-05) and Finnish Academy COLD Consortium (No. 322430).

550

551 **References**

- 552 Adusumilli, S., Fricker, H. A., Medley, B., Padman, L., and Siegfried, M. R.:
553 Interannual variations in meltwater input to the Southern Ocean from Antarctic ice
554 shelves, *Nat. Geosci.*, 13, 616–620, <https://doi.org/10.1038/s41561-020-0616-z>,
555 2020.
- 556 An, M., Wiens, D. A., Zhao, Y., Feng, M., Nyblade, A., Kanao, M., Li, Y., Maggi, A.,
557 and L ev eque, J.: Temperature, lithosphere-asthenosphere boundary, and heat flux
558 beneath the Antarctic Plate inferred from seismic velocities, *J. Geophys. Res. Solid*
559 *Earth*, 120, 8720–8742, <https://doi.org/10.1002/2015JB011917>, 2015.
- 560 Bell, R. E., Studinger, M., Shuman, C. A., Fahnestock, M. A., and Joughin, I.: Large



- 561 subglacial lakes in East Antarctica at the onset of fast-flowing ice streams, *Nature*,
562 445, 904–907, <https://doi.org/10.1038/nature05554>, 2007.
- 563 Chen, J. L., Wilson, C. R., Blankenship, D., and Tapley, B. D.: Accelerated Antarctic
564 ice loss from satellite gravity measurements, *Nature Geosci*, 2, 859–862,
565 <https://doi.org/10.1038/ngeo694>, 2009.
- 566 Comiso, J. C.: Variability and Trends in Antarctic Surface Temperatures from In Situ
567 and Satellite Infrared Measurements, *J. Climate*, 13, 1674–1696,
568 [https://doi.org/10.1175/1520-0442\(2000\)013<1674:VATIAS>2.0.CO;2](https://doi.org/10.1175/1520-0442(2000)013<1674:VATIAS>2.0.CO;2), 2000.
- 569 Cuffey, K. M., and Paterson, W. S. B.: *The physics of glaciers*, fourth edition, Elsevier,
570 Burlington, 2010.
- 571 Dow, C. F., McCormack, F. S., Young, D. A., Greenbaum, J. S., Roberts, J. L., and
572 Blankenship, D. D.: Totten Glacier subglacial hydrology determined from
573 geophysics and modeling, *Earth and Planetary Science Letters*, 531, 115961,
574 <https://doi.org/10.1016/j.epsl.2019.115961>, 2020.
- 575 Dow, Christine. Aurora Subglacial Basin GlADs inputs, outputs and geophysical data
576 [data set]. Zenodo. <https://doi.org/10.5281/zenodo.3525474>, 2019
- 577 Eisen, O., Winter, A., Steinhage, D., Kleiner, T., and Humbert, A.: Basal roughness of
578 the East Antarctic Ice Sheet in relation to flow speed and basal thermal state, *Ann.*
579 *Glaciol.*, 61, 162–175, <https://doi.org/10.1017/aog.2020.47>, 2020.
- 580 Fricker, H. A., Siegfried, M. R., Carter, S. P., and Scambos, T. A.: A decade of progress
581 in observing and modelling Antarctic subglacial water systems, *Phil. Trans. R. Soc.*
582 *A.*, 374, 20140294, <https://doi.org/10.1098/rsta.2014.0294>, 2016.
- 583 Gagliardini, O., Zwinger, T., Gillet-Chaulet, F., Durand, G., Favier, L., de Fleurian, B.,
584 Greve, R., Malinen, M., Martín, C., Råback, P., Ruokolainen, J., Sacchettini, M.,
585 Schäfer, M., Seddik, H., and Thies, J.: Capabilities and performance of Elmer/Ice,
586 a new-generation ice sheet model, *Geosci. Model Dev.*, 6, 1299–1318,
587 <https://doi.org/10.5194/gmd-6-1299-2013>, 2013.
- 588 Geuzaine, C. and Remacle, J.-F.: Gmsh: A 3-D finite element mesh generator with built-
589 in pre- and post-processing facilities: THE GMSH PAPER, *Int. J. Numer. Meth.*
590 *Engng.*, 79, 1309–1331, <https://doi.org/10.1002/nme.2579>, 2009.
- 591 Gillet-Chaulet, F., Gagliardini, O., Seddik, H., Nodet, M., Durand, G., Ritz, C., Zwinger,
592 T., Greve, R., and Vaughan, D. G.: Greenland ice sheet contribution to sea-level
593 rise from a new-generation ice-sheet model, *The Cryosphere*, 6, 1561–1576,
594 <https://doi.org/10.5194/tc-6-1561-2012>, 2012.
- 595 Greve R, Blatter H, *Dynamics of Ice Sheets and Glaciers*, Springer, 2009.
- 596 Gudlaugsson, E., Humbert, A., Andreassen, K., Clason, C. C., Kleiner, T., and Beyer,
597 S.: Eurasian ice-sheet dynamics and sensitivity to subglacial hydrology, *J. Glaciol.*,
598 63, 556–564, <https://doi.org/10.1017/jog.2017.21>, 2017.
- 599 Hansen, I. and Greve, R.: Polythermal modelling of steady states of the Antarctic ice
600 sheet in comparison with the real world, n.d.
- 601 Kang, H., Zhao, L., Wolovick, M., and Moore, J. C.: Evaluation of six geothermal heat
602 flux maps for the Antarctic Lambert–Amery glacial system, *The Cryosphere*, 16,
603 3619–3633, <https://doi.org/10.5194/tc-16-3619-2022>, 2022.
- 604 Larour, E., Seroussi, H., Morlighem, M., and Rignot, E.: Continental scale, high order,



- 605 high spatial resolution, ice sheet modeling using the Ice Sheet System Model
606 (ISSM): ICE SHEET SYSTEM MODEL, *J. Geophys. Res.*, 117, n/a-n/a,
607 <https://doi.org/10.1029/2011JF002140>, 2012a.
- 608 Larour, E., Morlighem, M., Seroussi, H., Schiermeier, J., and Rignot, E.: Ice flow
609 sensitivity to geothermal heat flux of Pine Island Glacier, Antarctica: ICE FLOW
610 SENSITIVITY TO GEOTHERMAL HEAT, *J. Geophys. Res.*, 117, n/a-n/a,
611 <https://doi.org/10.1029/2012JF002371>, 2012b.
- 612 Le Brocq, A. M., Payne, A. J., and Vieli, A.: An improved Antarctic dataset for high
613 resolution numerical ice sheet models (ALBMAP v1), *Earth Syst. Sci. Data*, 2,
614 247–260, <https://doi.org/10.5194/essd-2-247-2010>, 2010.
- 615 Le Brocq, A. M., Ross, N., Griggs, J. A., Bingham, R. G., Corr, H. F. J., Ferraccioli, F.,
616 Jenkins, A., Jordan, T. A., Payne, A. J., Rippin, D. M., and Siegert, M. J.: Evidence
617 from ice shelves for channelized meltwater flow beneath the Antarctic Ice Sheet,
618 *Nature Geosci*, 6, 945–948, <https://doi.org/10.1038/ngeo1977>, 2013.
- 619 Li, X., Rignot, E., Mouginot, J., and Scheuchl, B.: Ice flow dynamics and mass loss of
620 Totten Glacier, East Antarctica, from 1989 to 2015: TOTTEN GLACIER:
621 VELOCITY AND MASS CHANGE, *Geophys. Res. Lett.*, 43, 6366–6373,
622 <https://doi.org/10.1002/2016GL069173>, 2016.
- 623 Livingstone, S. J., Utting, D. J., Ruffell, A., Clark, C. D., Pawley, S., Atkinson, N., and
624 Fowler, A. C.: Discovery of relict subglacial lakes and their geometry and
625 mechanism of drainage, *Nat Commun*, 7, ncomms11767,
626 <https://doi.org/10.1038/ncomms11767>, 2016.
- 627 Livingstone, S. J., Li, Y., Rutishauser, A., Sanderson, R. J., Winter, K., Mikucki, J. A.,
628 Björnsson, H., Bowling, J. S., Chu, W., Dow, C. F., Fricker, H. A., McMillan, M.,
629 Ng, F. S. L., Ross, N., Siegert, M. J., Siegfried, M., and Sole, A. J.: Subglacial
630 lakes and their changing role in a warming climate, *Nat Rev Earth Environ*, 3,
631 106–124, <https://doi.org/10.1038/s43017-021-00246-9>, 2022.
- 632 Martos, Y. M., Catalán, M., Jordan, T. A., Golynsky, A., Golynsky, D., Eagles, G., and
633 Vaughan, D. G.: Heat Flux Distribution of Antarctica Unveiled, *Geophys. Res.*
634 *Lett.*, 44, 11,417–11,426, <https://doi.org/10.1002/2017GL075609>, 2017.
- 635 Maule, C. F., Purucker, M. E., Olsen, N., and Mosegaard, K.: Heat Flux Anomalies in
636 Antarctica Revealed by Satellite Magnetic Data, *Science*, 309, 464–467,
637 <https://doi.org/10.1126/science.1106888>, 2005.
- 638 Morlighem, M., Rignot, E., Seroussi, H., Larour, E., Ben Dhia, H., and Aubry, D.:
639 Spatial patterns of basal drag inferred using control methods from a full-Stokes
640 and simpler models for Pine Island Glacier, West Antarctica: SPATIAL
641 PATTERNS OF BASAL DRAG, *Geophys. Res. Lett.*, 37, n/a-n/a,
642 <https://doi.org/10.1029/2010GL043853>, 2010.
- 643 Mouginot, J., Scheuchl, B., and Rignot, E.: MEaSURES Antarctic Boundaries for IPY
644 2007-2009 from Satellite Radar, Version 2, National Snow and Ice Data Center,
645 10, <https://doi.org/doi.org/10.5067/AXE4121732AD>, 2017.
- 646 Pattyn, F.: Antarctic subglacial conditions inferred from a hybrid ice sheet/ice stream
647 model, *Earth and Planetary Science Letters*, 295, 451–461,
648 <https://doi.org/10.1016/j.epsl.2010.04.025>, 2010.



- 649 Pittard, M. L., Roberts, J. L., Galton-Fenzi, B. K., and Watson, C. S.: Sensitivity of the
650 Lambert-Amery glacial system to geothermal heat flux, *Ann. Glaciol.*, 57, 56–68,
651 <https://doi.org/10.1017/aog.2016.26>, 2016.
- 652 Pollack, H. N., Hurter, S. J., and Johnson, J. R.: Heat flow from the Earth’s interior:
653 Analysis of the global data set, *Rev. Geophys.*, 31, 267,
654 <https://doi.org/10.1029/93RG01249>, 1993.
- 655 Pritchard, H. D., Arthern, R. J., Vaughan, D. G., and Edwards, L. A.: Extensive dynamic
656 thinning on the margins of the Greenland and Antarctic ice sheets, *Nature*, 461,
657 971–975, <https://doi.org/10.1038/nature08471>, 2009.
- 658 Purucker, M.: Geothermal heat flux data set based on low resolution observation
659 collected by the CHAMP satellite between 2000 and 2010, and produced from
660 the MF-6 model following the technique described in Fox Maule et al. (2005),
661 Inter-active System for Ice sheet Simulation [data set],
662 http://websrv.cs.umt.edu/isis/index.php/Antarctica_Basal_Heat_Flux (last access:
663 5 August 2022), 2012.
- 664 Roberts, J., Galton-Fenzi, B. K., Paolo, F. S., Donnelly, C., Gwyther, D. E., Padman, L.,
665 Young, D., Warner, R., Greenbaum, J., Fricker, H. A., Payne, A. J., Cornford, S.,
666 Le Brocq, A., van Ommen, T., Blankenship, D., and Siegert, M. J.: Ocean forced
667 variability of Totten Glacier mass loss, *SP*, 461, 175–186,
668 <https://doi.org/10.1144/SP461.6>, 2018.
- 669 Rutishauser, A., Blankenship, D. D., Young, D. A., Wolfenbarger, N. S., Beem, L. H.,
670 Skidmore, M. L., Dubnick, A., and Criscitiello, A. S.: Radar sounding survey over
671 Devon Ice Cap indicates the potential for a diverse hypersaline subglacial
672 hydrological environment, *The Cryosphere*, 16, 379–395,
673 <https://doi.org/10.5194/tc-16-379-2022>, 2022.
- 674 Schroeder, D. M., Blankenship, D. D., and Young, D. A.: Evidence for a water system
675 transition beneath Thwaites Glacier, West Antarctica, *Proc. Natl. Acad. Sci. U.S.A.*,
676 110, 12225–12228, <https://doi.org/10.1073/pnas.1302828110>, 2013.
- 677 Schroeder, D. M., Blankenship, D. D., Raney, R. K., and Grima, C.: Estimating
678 Subglacial Water Geometry Using Radar Bed Echo Specularity: Application to
679 Thwaites Glacier, West Antarctica, *IEEE Geosci. Remote Sensing Lett.*, 12, 443–
680 447, <https://doi.org/10.1109/LGRS.2014.2337878>, 2015.
- 681 Shapiro, N.: Inferring surface heat flux distributions guided by a global seismic model:
682 particular application to Antarctica, *Earth and Planetary Science Letters*, 223, 213–
683 224, <https://doi.org/10.1016/j.epsl.2004.04.011>, 2004.
- 684 Shen, W., Wiens, D. A., Lloyd, A. J., and Nyblade, A. A.: A Geothermal Heat Flux Map
685 of Antarctica Empirically Constrained by Seismic Structure, *Geophysical*
686 *Research Letters*, 47, <https://doi.org/10.1029/2020GL086955>, 2020.
- 687 Stearns, L. A., Smith, B. E., and Hamilton, G. S.: Increased flow speed on a large East
688 Antarctic outlet glacier caused by subglacial floods, *Nature Geosci.*, 1, 827–831,
689 <https://doi.org/10.1038/ngeo356>, 2008.
- 690 Studinger, M., Bell, R. E., Kerner, G. D., Tikku, A. A., Holt, J. W., Morse, D. L., Richter,
691 T. G., Kempf, S. D., Peters, M. E., Blankenship, D. D., Sweeney, R. E., and
692 Rystrom, V. L.: Ice cover, landscape setting, and geological framework of Lake



- 693 Vostok, East Antarctica, *Earth and Planetary Science Letters*, 205, 195–210,
694 [https://doi.org/10.1016/S0012-821X\(02\)01041-5](https://doi.org/10.1016/S0012-821X(02)01041-5), 2003.
- 695 Talalay, P., Li, Y., Augustin, L., Clow, G. D., Hong, J., Lefebvre, E., Markov, A.,
696 Motoyama, H., and Ritz, C.: Geothermal heat flux from measured temperature
697 profiles in deep ice boreholes in Antarctica, *The Cryosphere*, 14, 4021–4037,
698 <https://doi.org/10.5194/tc-14-4021-2020>, 2020.
- 699 Van Liefferinge, B. and Pattyn, F.: Using ice-flow models to evaluate potential sites of
700 million year-old ice in Antarctica, *Clim. Past*, 9, 2335–2345,
701 <https://doi.org/10.5194/cp-9-2335-2013>, 2013.
- 702 Van Liefferinge, B., Pattyn, F., Cavitte, M. G. P., Karlsson, N. B., Young, D. A., Sutter,
703 J., and Eisen, O.: Promising Oldest Ice sites in East Antarctica based on
704 thermodynamical modelling, *The Cryosphere*, 12, 2773–2787,
705 <https://doi.org/10.5194/tc-12-2773-2018>, 2018.
- 706 Wolovick, M. J., Moore, J. C., and Zhao, L.: Joint Inversion for Surface Accumulation
707 Rate and Geothermal Heat Flow From Ice-Penetrating Radar Observations at
708 Dome A, East Antarctica. Part I: Model Description, Data Constraints, and
709 Inversion Results, *JGR Earth Surface*, 126, <https://doi.org/10.1029/2020JF005937>,
710 2021a.
- 711 Wolovick, M. J., Moore, J. C., and Zhao, L.: Joint Inversion for Surface Accumulation
712 Rate and Geothermal Heat Flow From Ice-Penetrating Radar Observations at
713 Dome A, East Antarctica. Part II: Ice Sheet State and Geophysical Analysis, *JGR*
714 *Earth Surface*, 126, <https://doi.org/10.1029/2020JF005936>, 2021b.
- 715 Wright, A. and Siegert, M.: A fourth inventory of Antarctic subglacial lakes, *Antarctic*
716 *Science*, 24, 659–664, <https://doi.org/10.1017/S095410201200048X>, 2012.
- 717 Wright, A. P., Young, D. A., Roberts, J. L., Schroeder, D. M., Bamber, J. L., Dowdeswell,
718 J. A., Young, N. W., Le Brocq, A. M., Warner, R. C., Payne, A. J., Blankenship, D.
719 D., van Ommen, T. D., and Siegert, M. J.: Evidence of a hydrological connection
720 between the ice divide and ice sheet margin in the Aurora Subglacial Basin, East
721 Antarctica, *J. Geophys. Res.*, 117, 2011JF002066,
722 <https://doi.org/10.1029/2011JF002066>, 2012.
- 723 Young, D. A., Schroeder, D. M., Blankenship, D. D., Kempf, S. D., and Quartini, E.:
724 The distribution of basal water between Antarctic subglacial lakes from radar
725 sounding, *Phil. Trans. R. Soc. A.*, 374, 20140297,
726 <https://doi.org/10.1098/rsta.2014.0297>, 2016.
- 727 Zhao, C., Gladstone, R. M., Warner, R. C., King, M. A., Zwinger, T., and Morlighem,
728 M.: Basal friction of Fleming Glacier, Antarctica – Part 1: Sensitivity of inversion
729 to temperature and bedrock uncertainty, *The Cryosphere*, 12, 2637–2652,
730 <https://doi.org/10.5194/tc-12-2637-2018>, 2018.

731